Genetic optimization of carbon fiber cross-sections for tailorable compressive properties

Pranav Rane[a], Cordelia Latham[b], Michael Czabaj[b]

[a]Department of Mechanical and Civil Engineering, California Institute of Technology, Pasadena, CA 91125
[b]Department of Mechanical Engineering, University of Utah, Salt Lake City, UT 84112

Abstract

Carbon-fiber reinforced polymer (CFRP) composites are widely used due to their high tensile strength and stiffness, yet their performance in compression-dominated applications remains limited. This work aims to enhance the compressive strength of CFRPs by optimizing the cross-sectional geometry of individual fibers. The approach is based on the premise that modifying the geometry of fiber cross-sections alters the buckling response of individual filaments, thereby delaying composite compressive failure initiated by fiber microbuckling. An evolutionary algorithm is employed to optimize symmetric, star-convex fiber cross-sections by maximizing the critical area moment of inertia, a geometric parameter directly related to buckling resistance and fiber waviness. The optimization identifies both solid and hollow tri-lobal geometries that exhibit significantly increased area moments of inertia compared to conventional circular fibers. Experimental validation using additively manufactured macroscale fiber analogs confirms the predicted improvements in compressive strength while maintaining comparable tensile properties, albeit with reduced fiber volume fraction. These findings demonstrate that tailored fiber cross-sectional geometries provide a viable pathway for improving the compressive performance of CFRP composites and enabling new design strategies for compression-critical applications.

1.0 Introduction

Carbon-fiber reinforced polymer (CFRP) composites are a class of lightweight, high-performance materials that have been widely adopted across key engineering sectors, including aerospace, energy, and automotive applications. Over decades of research and development, efforts have primarily focused on improving the tensile stiffness and strength of individual fiber filaments, as well as the toughness of the polymer matrix. The desire to continuously improve these properties is not without merit. For example, in many high-performance structural applications (e.g., airplane fuselage components, composite overwrapped pressure vessels, and other structures experiencing high tensile loads) the tensile stiffness and strength of the CFRP system drive the overall part sizing. Moreover, in nearly all composite structures regardless of loading type, matrix tensile fracture is often the first mode of failure to be observed, thus increasing matrix toughness is of high importance. Consequently, the focus on improving these properties has led to development of ultra-high-modulus (e.g., Toray M60J or Hexcel HM 63) and high-strength (e.g., Toray T1100G/S or Hexcel IM10) carbon fibers and highly toughened epoxy resins (e.g., Toray 3960 or Hexcel M91).

An unintended consequence of these developments has been a shift in structural design practices, where many CFRP components subjected to multi-axial loading are now sized based on fiber-direction compressive properties. As noted by Rousseau et al., improvements in compressive performance have been incremental and have not kept pace with advances in tensile stiffness and strength [2012_Rousseau]. As a result, unidirectional carbon fiber/epoxy laminates often exhibit compressive strengths up to three times lower than their tensile strengths [2023_Nunna].

Compressive failure in unidirectional fiber-reinforced composites generally occurs through four primary modes: fiber microbuckling, kinking, longitudinal cracking, and fiber fracture [1996_Schultheisz_Waas]. Among these, kinking is the most commonly observed and is often considered the final, irreversible stage following the progression of fiber microbuckling. Accordingly, delaying or preventing the onset of local fiber microbuckling represents a promising pathway for enhancing composite compressive strength. This may be achieved through improvements in matrix, fiber, and interfacial properties, as well as reductions in defects such as fiber misalignment.

The relationship between matrix properties and microbuckling has been extensively studied over the past several decades. Rosen et al. were among the first to analyze microbuckling, showing that compressive strength is proportional to the shear modulus of the matrix [1965_Rosen]. Subsequent studies expanded on this work by incorporating additional factors such as fiber misalignment and matrix nonlinearity [1972_Argon; 1983_Budiansky; 1990_Fleck; 1994_Sun; 2009_Pimenta_1]. Uddin et al. developed an epoxy matrix reinforced with silica nanoparticles, resulting in a 40% increase in matrix modulus and over a 60% increase in longitudinal compressive strength [2008_Uddin]. More recently, Lu et al. designed a high-modulus epoxy system using grafted silica and evaluated the resulting compressive strength through analytical and experimental approaches [2022_Lu]. Their results showed that increasing matrix modulus delayed fiber microbuckling, leading to over a 15% improvement in longitudinal compressive strength. Similarly, Makeev et al. demonstrated that incorporating nanoscale reinforcements in the matrix, combined with hybrid carbon fiber systems, resulted in more than a 10% increase in compressive strength compared to conventional high-modulus CFRPs [2019_Makeev].

Microbuckling is strongly influenced by two fiber properties: (1) the buckling resistance of individual fibers and (2) the degree of initial fiber misalignment. To examine the former, Euler column buckling theory provides a linear elastic model for predicting instability in perfectly straight fibers:

$$F_{cr} = \frac{\pi^2 EI}{(KL)^2}. \tag{1.1}$$

where, F_{cr} is the critical buckling load, E is the fiber modulus, L is the unsupported length of the fiber, and K is a factor accounting for boundary conditions. The area moment of inertia, I, is a geometric property of the fiber cross-section, which, for sufficiently symmetric cross-sections, is defined as:

$$I = \frac{1}{2}\int r^2 dA, \tag{1.2}$$

where r is the distance from the centroid and A is the cross-sectional area.

The degree of initial fiber misalignment (specifically local fiber waviness) is governed by the flexural rigidity (EI) of the fibers, as well as deformation and entanglement during fiber production and composite cure. The flexural response of individual fibers can be approximated using the beam deflection formula in the form of an ordinary differential equation,

$$\frac{d^2 v}{dx^2} = \frac{M(x)}{EI}, \tag{1.3}$$

where v is the beam deflection, x is the spatial coordinate along the fiber length, and M is the applied bending moment. The reduction in the buckling load due to geometric imperfections can be described using, for example, the secant buckling formula derived from Eq. 1.3.

Examining Eqs. 1.1 and 1.3, and assuming that deformation of individual fibers can be approximated using classical buckling and beam theories, the onset of fiber buckling is proportional to EI, while fiber curvature (waviness) is inversely proportional to the same quantity. Thus, both the critical buckling load and the sensitivity to fiber waviness are governed by the flexural rigidity of the fibers. For a given material system, this highlights the area moment of inertia, I, as a key geometric parameter controlling compressive behavior. Several studies on composite compressive failure have incorporated fiber flexural rigidity into their analyses. Xu et al. developed a micromechanical beam-on-elastic-foundation model in which the predicted buckling wavelength depends on fiber flexural rigidity and matrix stiffness [1993_Xu]. Similarly, Gardin et al. derived an expression indicating that composite compressive strength is proportional to fiber flexural rigidity [2002_Gardin]. More recently, Pimenta et al. proposed a model for longitudinal compressive strength that scales with fiber flexural rigidity and showed strong agreement with numerical simulations [2009_Pimenta_2].

Many efforts have focused on improving composite compressive performance by increasing the fiber modulus, E. These efforts have led to the development of standard and intermediate modulus (SM and IM) carbon fibers (200–350 GPa), as well as high and ultra-high modulus (HM and UHM) fibers (350–600 GPa). Experimental studies have shown that, for SM and IM fibers, increases in modulus correlate with improvements in composite compressive strength, consistent with the models described previously [2023_Nunna; 2012_Rousseau]. However, further increases in modulus in HM and UHM fibers can lead to a transition in failure mode from fiber microbuckling to fiber splitting, resulting in a reduction in compressive strength [2023_Nunna; 2012_Rousseau].

In contrast, comparatively fewer studies have focused on increasing I. Most commercial carbon fibers have circular or near-circular cross-sections with diameters on the order of 5–8 μm [2020_Toray]. Over two decades ago, Bond et al. compared composites reinforced with circular and triangular glass fibers and reported over a 40% improvement in compressive strength for triangular cross-sections [2002_Bond]. This improvement was partly attributed to a 16.9% increase in I relative to circular fibers. While it is known that an equilateral triangle maximizes I among convex cross-sections [1960_Keller], non-convex geometries offer the potential for even greater increases. More recently, Ennis et al. optimized a family of star-convex, lobular carbon fiber cross-sections to maximize I while also considering shape perimeter, manufacturing cost, and fiber volume fraction [2022_Ennis]. Their parameterized representation was limited to four geometric variables, restricting the accessible design space. Nevertheless, one optimized six-lobed design achieved a 62% increase in I relative to a circular cross-section, corresponding to a predicted 10–13% improvement in composite compressive strength [2023_Camarena]. While these results demonstrate the potential of noncircular geometries, the restricted parameterization limits exploration of more general cross-sectional shapes.

In the context of the preceding discussion and prior work by Ennis et al. [2022_Ennis], the primary objective of this study is to optimize fiber cross-sectional geometry within an expanded design space to directly maximize I. A genetic algorithm is employed to optimize a vector of design variables that is mapped to the cross-sectional boundary, enabling the exploration of star-convex geometries with D_3 symmetry (120° rotational and reflectional symmetry). An additional design variable defines the radius of a central hole, allowing for the investigation of hollow cross-sections that further increase I by redistributing material away from the centroid. Four geometric constraints are enforced to regulate cross-sectional area, feature aspect ratio, hole size, and minimum structural thickness. As a validation step, convexity is temporarily imposed as an additional constraint, for which the optimal solution is expected to be an equilateral triangle. To evaluate the mechanical implications of the optimized geometries, macroscale fiber analogs are additively manufactured and tested under both compression and tension. Fiber volume fraction, a key parameter in composite performance, is assessed through experimental packing studies. In addition to identifying geometries with enhanced I, this work establishes a generalizable optimization framework that can be extended to multi-objective problems involving competing metrics such as fiber volume fraction, interfacial surface area, and manufacturing cost. The framework is also adaptable to cross-sections with arbitrary dihedral symmetry, providing flexibility in exploring a wide range of geometric configurations. While the present study focuses on carbon fibers, the methodology is broadly applicable to other fiber systems or structural concepts susceptible to compressive failure.

The following sections describe the optimization framework used to generate carbon fiber cross-sections with near-optimal I, followed by validation procedures, problem parameters, and experimental methods for mechanical testing and packing studies. The paper concludes with an analysis of the theoretical, numerical, and experimental buckling performance of the optimized cross-sections, along with corresponding estimates of fiber volume fraction.

2.0 Optimization Framework

2.1 Objective function

The objective of this study is to optimize the cross-sectional geometry of fibers to maximize I, which, as discussed in the Introduction, is a key geometric parameter governing fiber buckling and composite compressive failure. Given a cross-sectional boundary described by vertices (x_i, y_i) in a 2D Cartesian system (with the origin located at the centroid), the area moments of inertia along the *x*- and *y*-axes are computed as discreate sum over the boundary [1984_Marín]

$$I_{xx} = \frac{1}{12}\sum w_i[(y_i + y_{i+1})^2 - y_i y_{i+1}] \tag{2.1}$$

$$I_{yy} = \frac{1}{12}\sum w_i[(x_i + x_{i+1})^2 - x_i x_{i+1}] \tag{2.2}$$

where $w_i = x_i y_{i+1} - x_{i+1} y_i$. Similarly, the product of inertia can be computed as:

$$I_{xy} = \frac{1}{24}\sum w_i[(x_i + x_{i+1})\,(y_i + y_{i+1}) + x_i y_i + x_{i+1} y_{i+1}]. \tag{2.3}$$

The two principal components of the area moment of inertia, I_1 and I_2, can be computed as:

$$I_1, I_2 = \mathrm{eig}\left(\begin{bmatrix} I_{xx} & I_{xy} \\ I_{xy} & I_{yy} \end{bmatrix}\right), \tag{2.4}$$

where I_2 is smaller eigenvalue, which, for general 3D column buckling, governs the magnitude of F_{cr}. Accordingly, the primary aim of the optimization framework is to maximize I_2, as stated by the objective function:

$$\max_{\boldsymbol{x}} I_2(\boldsymbol{x}), \tag{2.5}$$

where $\boldsymbol{x}$ is the vector of design variables that maps to the geometric vertices (x_i, y_i) of the cross-section boundary, subjected to the geometric constraints described in the following sections.

2.2 Cross-section representation

The cross-section representation defines how the vector of design variables, $\boldsymbol{x}$, is transformed into the cross-section geometry. One cross-section representation explored in preliminary studies mapped $\boldsymbol{x}$ to a set of vertices defined in a polar coordinate system, enabling the exploration of star-convex shapes. Star-convex shapes are defined as geometries for which there exists at least one interior point from which a line can be drawn to every boundary vertex without intersecting the boundary. This class of shapes lies between purely convex and fully concave geometries, allowing the optimization of non-convex cross-sections while avoiding the geometric complexity associated with unrestricted concave shapes.

While restricting the design space to star-convex geometries improves computational tractability, certain geometries remain inaccessible, as illustrated in Figure 1a. Preliminary optimization using this representation and the objective function defined in Eq. 2.5 resulted in cross-sections exhibiting a tri-lobal geometry, characterized by three identical protruding lobes spanning 120°. These optimized geometries exhibited dihedral (D_3) symmetry, consisting of 120° rotational and reflectional symmetry, depicted in Figure 1b. However, increasing the number of design variables, and therefore the number of vertices, to increase the boundary resolution, led to convergence difficulties due to high dimensionality of the design space. Consequently, the representation was modified to explicitly incorporate the observed D_3 symmetry, thereby reducing the number of design variables while preserving the ability to capture optimal geometries.

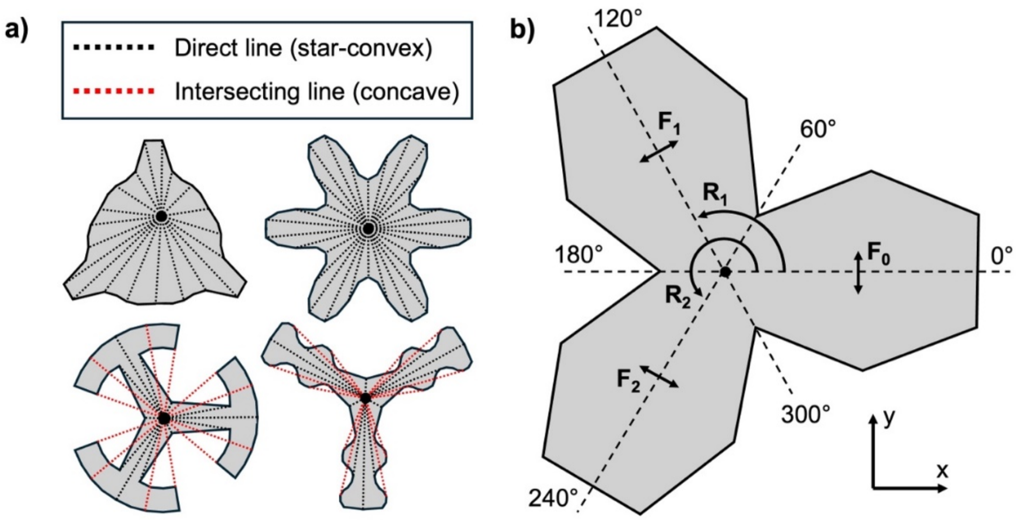

Figure 1: **(a)** Examples of star-convex and non-star-convex D_3 cross-sections. The top two cross-sections are star-convex, as there exists an interior point from which a line can be drawn to each boundary vertex without intersecting the boundary. The bottom two cross-sections do not satisfy this condition and are therefore not star convex. **(b)** Example cross-section with D_3 symmetry, illustrating F_j and R_j reflectional and rotational symmetries, respectively, about $\theta = 120j$ degrees ($j = 0,1,$ and 2).

The dihedral group D_n contains the symmetries of an n-gon (e.g. an equilateral triangle, square, pentagon, etc.) and consists of n rotational and n reflectional symmetries, which can be expressed as linear transformations acting on the boundary vertices. These transformations are given by:

$$R_k = \begin{bmatrix} \cos\left(\frac{2\pi k}{n}\right) & -\sin\left(\frac{2\pi k}{n}\right) \\ \sin\left(\frac{2\pi k}{n}\right) & \cos\left(\frac{2\pi k}{n}\right) \end{bmatrix}, \tag{2.6}$$

$$F_k = \begin{bmatrix} \cos\left(\frac{2\pi k}{n}\right) & \sin\left(\frac{2\pi k}{n}\right) \\ \sin\left(\frac{2\pi k}{n}\right) & -\cos\left(\frac{2\pi k}{n}\right) \end{bmatrix}, \tag{2.7}$$

where the first transformation represents a counterclockwise rotation through an angle $\theta = 2\pi k/n$, and the second represents reflection about a line angled at $\theta = \pi k/n$ from the x-axis, for $k = 0,1, \dots, n$. This symmetry is incorporated into the cross-sectional representation through a radial vector $\boldsymbol{r}$ of size N, which stores radial coordinates of a portion of the boundary in polar form. The corresponding angular components are evenly spaced and, for D_n symmetry, are given by:

$$\theta_i = \frac{90}{Nn}(2i - 1) \tag{2.8}$$

where $i = 1,2,\dots,N$. The vertices $(\boldsymbol{r},\ \boldsymbol{\theta})$ define the cross-sectional boundary between 0°-$(180/n)$°, which is depicted for $n = 3$ in Figure 2a. The radial vector $\boldsymbol{r}_{\text{full}}$, of size $2Nn$, is constructed as:

$$\boldsymbol{r}_{\text{full}} = \underbrace{[\boldsymbol{r}, \boldsymbol{r}_{\text{flip}}]}_{\text{repeated } n \text{ times}} = [\boldsymbol{r}, \boldsymbol{r}_{\text{flip}}, \boldsymbol{r}, \boldsymbol{r}_{\text{flip}}, \cdots, \boldsymbol{r}, \boldsymbol{r}_{\text{flip}}] \tag{2.9}$$

where $\boldsymbol{r}_{\text{flip}}$ is the flipped version of $\boldsymbol{r}$, as illustrated in Figure 2b. The corresponding angular coordinates of the full cross-section are stored in $\boldsymbol{\theta}_{\text{full}}$ and are computed using Eq. 2.8 for $i = 1, 2, \dots, 2Nn$. The resulting set of vertices $(\boldsymbol{r}_{\text{full}}, \boldsymbol{\theta}_{\text{full}})$ define the entire cross-section, as shown in Figure 2c. In this study, $n = 3$, restricting the design space to star-convex geometries with D_3 symmetry.

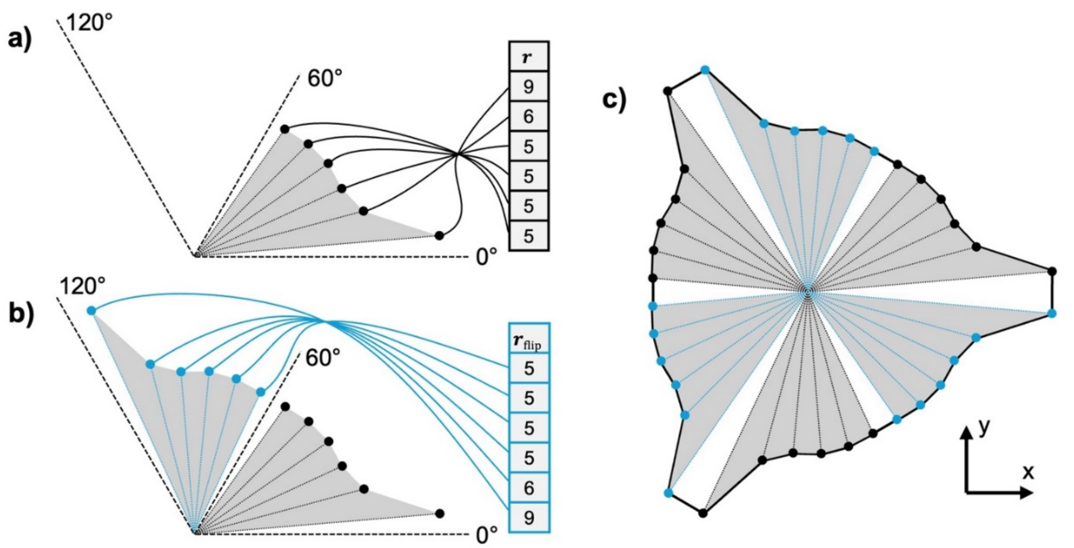

Figure 2: a) The radial vector $\boldsymbol{r}$ plotted with corresponding angular coordinates for $n = 3$, given by Eq. 2.8. b) The flipped radial vector $\boldsymbol{r}_{\text{flip}}$ which creates a symmetric extension of $\boldsymbol{r}$. c) Full radial and angular vectors, $(\boldsymbol{r}_{\text{full}}, \boldsymbol{\theta}_{\text{full}})$, plotted to construct the complete cross-section boundary with D_3 symmetry.

2.2.1 Hollow cross-sections

In addition to optimizing the outer cross-sectional boundary, hollow geometries are explored by introducing a centered circular hole of radius r_{hole}. The inclusion of a hollow region enables redistribution of material away from the origin, thereby increasing I_2 while maintaining cross-sectional area, or alternatively, maintaining I_2 while decreasing the cross-sectional area. Recent studies have demonstrated that hollow carbon fibers are manufacturable and can provide enhanced composite properties [2012_Tsotsis, 2015_Gulgunje, 2021_Shirolkar]. Accordingly, the full vector of design variables, $\boldsymbol{x}$, is defined as

$$\boldsymbol{x} = [\boldsymbol{r}, r_{\mathrm{hole}}]. \tag{2.10}$$

2.3 Explicit cross-section constraints

The cross-section representation implicitly enforces star-convexity and D_3 symmetry. However, additional control over specific geometric features—namely (1) cross-sectional area, (2) narrow features, (3) hole size, and (4) structural thickness—is introduced through explicit constraints. These parameters are illustrated in Figure 3 and are described below. The constraint on cross-sectional area is necessary due to the form of the objective function. For a given cross-section, I_2 can be increased either by increasing the total area or by redistributing material further from the centroid. By enforcing a fixed cross-sectional area constraint, the optimization focuses on geometry rather than size. The area constraint for a cross-section $\boldsymbol{x}$ is defined as:

$$A(\boldsymbol{x}) = A_{\mathrm{desired}}, \tag{2.11}$$

where A_{desired} is the desired cross-sectional area. To enforce this constraint, a repair function is applied to scale every cross-section to A_{desired}. This is achieved by multiplying the elements of $\boldsymbol{r}$ by a scaling factor, s, given by:

$$s = \sqrt{\frac{A'}{A}} \tag{2.12}$$

where A is the current cross-sectional area and $A' = A_{\mathrm{desired}} + \pi r_{\mathrm{hole}}^2$ is the target cross-sectional area, accounting for the presence of a circular hole.

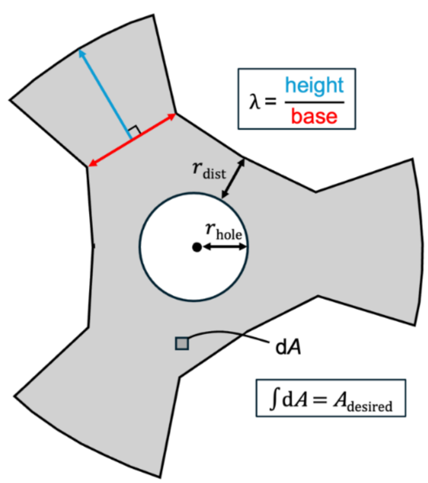

Figure 3: Visualization of the explicit geometric constraints on cross-sectional area, feature aspect ratio, hole radius, and structural thickness.

Cross-sections with sharp and narrow features are also constrained, as they will likely be difficult to manufacture and may lead to early compressive failure through local buckling. These features are identified using an aspect ratio metric, λ, defined for all geometric features in $\boldsymbol{r}$. High aspect ratio features indicate the presence of narrow regions, leading to the constraint

$$\lambda(\boldsymbol{r}) \leq \lambda_{\text{desired}}, \tag{2.13}$$

where λ_{desired} is the maximum allowable aspect ratio for any feature protruding from the cross-section. Efficient evaluation of feature aspect ratios is non-trivial; therefore, a brute force approach is adopted, as illustrated in Figure 4. For each vertex (r_i, θ_i), a collection of width-height pairs $\{(w_{i,j}, h_{i,j})\}_{j=1}^{6N}$ is computed. Here, $w_{i,j}$ corresponds to the line segment drawn from (r_i, θ_i) to (r_j, θ_j), and $h_{i,j}$ corresponds to a line segment drawn such that one endpoint touches $w_{i,j}$ perpendicularly, and the other endpoint either touches or aligns perpendicularly with the furthest available vertex in the feature. The aspect ratio $\lambda_{i,j}$ for each geometric feature is computed as the length of $h_{i,j}$ divided by the length of $w_{i,j}$. If $\lambda_{i,j} > \lambda_{\text{desired}}$, a high aspect ratio feature is present in the cross-section.

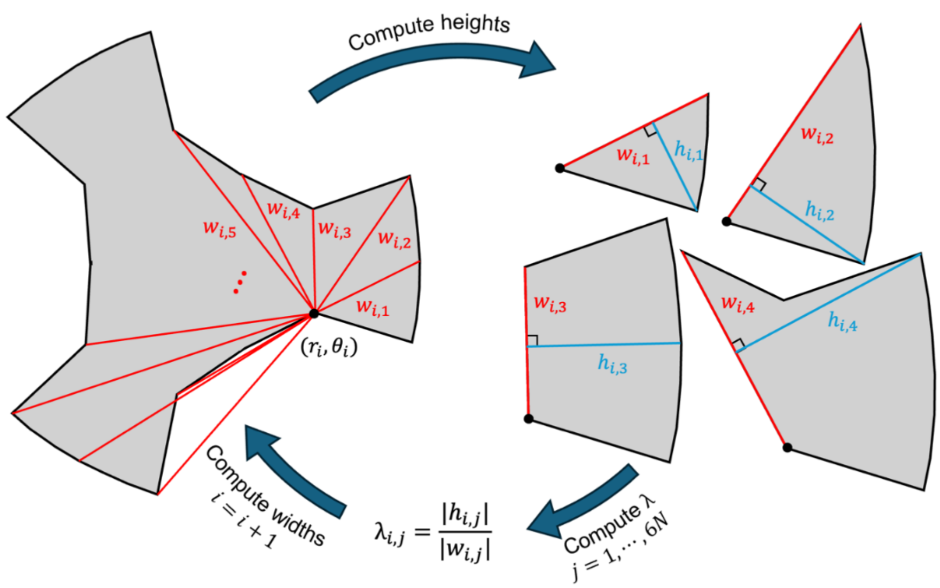

Figure 4: Schematic of the algorithm used to identify high aspect ratio geometric features. The widths and heights of each cross-sectional feature are computed to determine the associated aspect ratios.

For hollow cross-sections, the size of the hole is constrained by imposing an upper bound on the design variable, r_{hole}, defined as:

$$r_{\text{hole}} \leq R_{\text{hole}}, \tag{2.14}$$

where R_{hole} is the maximum desired hole radius.

Finally, a minimum structural thickness is enforced by preventing excessively thin regions that may fail during fiber or composite manufacturing. This is achieved by requiring a minimal radial thickness from the centroid to the outer boundary, given by $r_{\text{dist}} = \min(\boldsymbol{r} - r_{\text{hole}})$. The inequality constraint is then defined as:

$$r_{\text{dist}} \geq R_{\text{dist}}, \tag{2.15}$$

where R_{dist} is the minimum allowable radial thickness.

2.4 Genetic algorithm

A genetic algorithm (GA) is employed to solve the optimization problem due to the complex, multimodal and potentially discontinuous nature of the design space. As described previously, the framework maximizes the objective function (Eq. 2.5) subject to multiple geometric constraints (Eqs. 2.11-2.15), resulting in a high-dimensional search space that is not well suited for calculus-based or exhaustive optimization methods [1989_Goldberg]. Furthermore, the framework is designed to accommodate extensions to multi-objective optimization problems. Accordingly, a GA provides a robust and flexible approach for exploring large and constrained geometric design space.

GAs are inspired by principles of genetic and natural selection, and offer several advantages, including the ability to handle high-dimensional problems, operate without gradient information, and avoid convergence to local optima. In additional, GAs are well suited for parallel implementation and can be readily extended to multi-objective formulations [2004_Haupt]. In this work, the GA enables a large population of individual cross-sections to evolve over successive generations through genetic operators that recombine and modify advantageous geometric features to converge to a solution with maximum "fitness," determined by the objective function and constraint violations.

2.4.1 Fitness function

The fitness function guides the population of candidate solutions to maximize the objective function while minimizing constraint violations. Given a cross-section $\boldsymbol{x}$, the full polar vertices ($\boldsymbol{r}_{\text{full}}$, $\boldsymbol{\theta}_{\text{full}}$) are transformed to Cartesian coordinates $(\boldsymbol{x}, \boldsymbol{y})$ to evaluate I_2 (Eq. 2.4). For hollow cross-sections, a factor $(\pi/4)r_{\text{hole}}^4$, corresponding to the I_2 of the material replaced by the hollow center, is subtracted to obtain the correct value for I_2. The fitness function is then defined as:

$$f(\boldsymbol{x}) = \begin{cases} I_2(\boldsymbol{r}) - \dfrac{\pi}{4} r_{\text{hole}}^4, & \lambda(\boldsymbol{r}) \leq \lambda_{\text{desired}},\ r_{\text{dist}} \geq R_{\text{dist}}, \text{and } r_{\text{hole}} \leq R_{\text{hole}} \\ -\infty, & \text{else} \end{cases} \tag{2.16}$$

where violations of the constraints λ_{desired}, R_{dist}, or R_{hole} result in a cross-section with an infinitely poor fitness score. In the GA, the fitness scores of all individuals in the population are ranked at the start of each generation to enable selection of high-performing cross-sections that contribute to the next generation.

2.4.2 Initial population

The initial population P_0 contains of cross-sections with diverse geometric characteristics to ensure broad exploration of the design space and increase the likelihood of identifying a global optimum. To achieve this, a shape-generating function is designed to create a wide range of lobular cross-sections, given by:

$$r_i = \alpha \sin\left(\frac{\omega(i-\delta)}{N}\right) + 2\varphi, \tag{2.17}$$

where $i = 1,2, \ldots, N$. Initial radial vectors are generated by varying parameters α, ω, δ, and φ which control lobe length, the number of lobes, angular position of lobes, and the distance from the lobe base to the centroid, respectively. Additionally, r_{hole} for each initial cross-section is randomly selected within the range $[0, R_{\text{hole}}]$. The number of individuals in the population, P_{size}, remains constant during optimization and is determined by the size of the initial population.

2.4.3 Selection and genetic operators

After ranking the fitness of cross-sections at the start of each generation i, individuals are selected from the current population P_i to be altered through genetic operators—crossover and mutation—which pass desirable traits to the next generation while promoting diversity and preventing premature convergence to local optima. The new population P_{i+1} at generation $i+1$ consists of two groups: (1) $P_{\text{size}} \times p_c$ cross-sections generated by crossover and (2) $P_{\text{size}} \times (1 - p_c)$ cross-sections generated by mutation, where p_c is the crossover fraction in the range $[0,1]$.

The two genetic operators act on selected cross-sections from P_i. Cross-sections are selected through a tournament selection process, where four cross-sections are randomly chosen from P_i, and the one with the highest fitness score is selected. Each crossover operation requires two selected "parent" cross-sections, and each mutation operation requires one. Therefore, the tournament selection process is repeated with replacement until $2(P_{\text{size}} \times p_c) + P_{\text{size}} \times (1 - p_c)$ cross-sections are selected.

The crossover operator exchanges beneficial geometric features between two selected parent cross-sections. A two-point crossover function is used, where a random section of the radial vectors from each parent is swapped, as illustrated in Figure 5. The resulting two cross-sections, referred to as "child" cross-sections, are rescaled to achieve the desired cross-sectional area (Eq. 2.12) and feature a hole radius that is the average of their parents hole radii. Finally, one child cross-section is discarded at random, and the other is chosen to be in P_{i+1}.

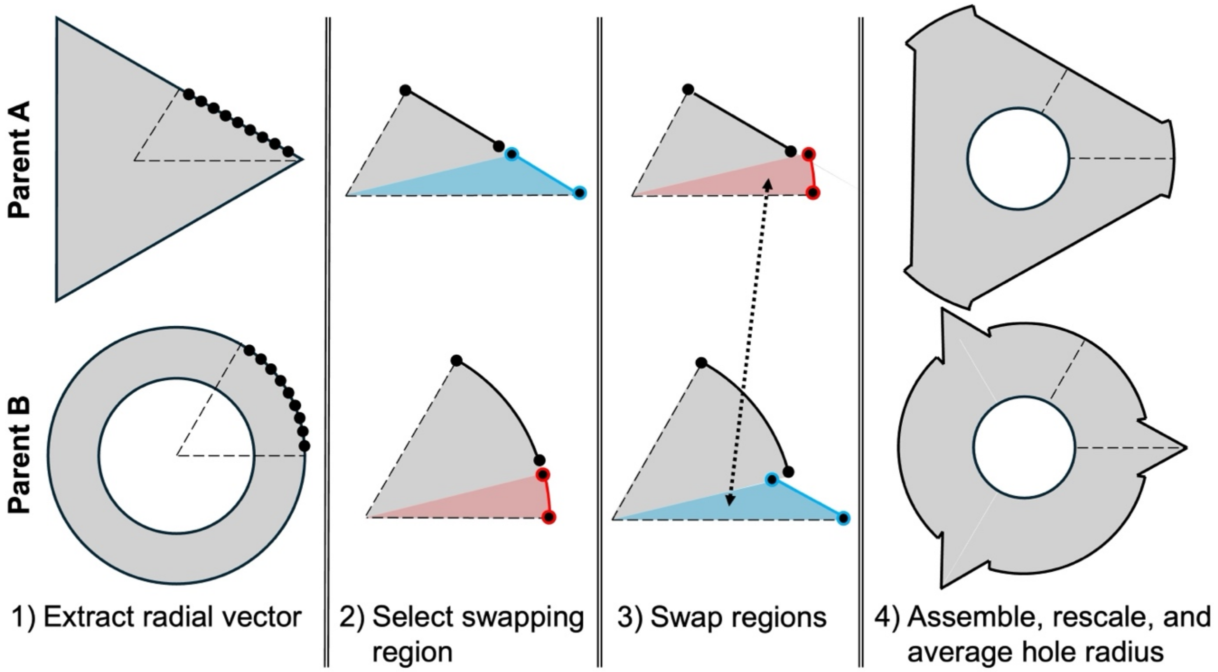

Figure 5: Illustration of the two-point crossover function used to pass geometric traits of selected parents. Two parent cross-sections with high fitness scores are selected and combined. One of the two child cross-sections is randomly selected for inclusion in the next generation.

For the mutation operator, $P_{\text{size}} \times (1 - p_c)$ cross-sections are selected in the same manner. The mutation operator randomly perturbs the components of $\boldsymbol{x}$ and introduces a probability for $\boldsymbol{r}$ to undergo circular rotation by a random amount. This promotes variability and diversification of cross-section shapes. As with the crossover operator, the final mutated cross-sections are rescaled to achieve the desired cross-sectional area.

2.4.4 Stopping condition

The GA cycles between evaluating the fitness of the population, selecting high-ranked cross-sections, and modifying geometric features for the next population. The optimization is set to terminate after 200 stall generations, where a stall generation is defined as one in which the cross-section with the highest fitness score remains unchanged.

3.0 Optimization Studies

Three studies are conducted using the GA, each with a specific objective: (1) algorithm validation, (2) solid star-convex optimization, and (3) hollow star-convex optimization. The validation study is designed to assess the algorithm against a problem with a known optimal solution. The second and third studies expand the design space to solid and hollow star-convex geometries, as motivated in the introduction. In all three studies, the GA is implemented using MATLAB's Global Optimization Toolbox and executed on a workstation equipped with an Intel Xeon CPU E5-2699 (44 cores, 2.20 GHz base clock) and 256 GB DDR4 RAM.

3.1 Validation study: convex optimization

The optimization framework is validated by introducing an additional constraint requiring all cross-sections to be convex. Successful convergence is indicated by a final solution corresponding to an equilateral triangle, which is known to maximize I_2 for convex 2D shapes. To enforce convexity, each cross-section generated after crossover and mutation is transformed by a repair function that replaces non-convex child cross-sections with their convex hull, thereby restricting the search space to convex shapes. Since an equilateral triangle is the optimal solution for all convex shapes, high aspect ratio features are permitted and do not require additional restriction. The problem parameters are listed in the first row of Table 3.1.

Table 3.1: Problem and algorithmic parameters used for the three optimization studies: convex, solid star-convex, and hollow star-convex. The listed parameters define the geometric constraints and genetic algorithm settings for each case.

	λ_{desired}	A_{desired}	R_{hole}	R_{dist}	N	p_c	P_{size}
Convex	∞	1	0	0	30	0.8	200
Solid	$1, 1.5, 2, 2.5, 3, 3.5, 4, 5$	1	0	0	30	0.8	4000
Hollow	$1, 1.5, 2, 2.5, 3, 3.5, 4, 5$	1	$0.1, 0.2$	0.1	30	0.8	4000

The algorithmic parameters are set to have a crossover fraction of $p_c = 0.8$ and a population size of $P_{\text{size}} = 200$. The crossover fraction was selected based on preliminary testing to balance exploration and exploitation. Lower values led to slower convergence due to increased mutation, while higher values resulted in premature convergence due to reduced mutation. The population size was determined through repeated runs of the GA with varying values of P_{size}, selecting a value that ensured convergence while remaining computationally feasible.

3.2 Solid star-convex optimization

The second study considers optimization of solid star-convex cross-sections with D_3 symmetry. To explore a range of geometries, the maximum allowable feature aspect ratio λ_{desired} is varied across eight runs. The corresponding problem parameters are listed in the second row of Table 3.1. The population size is selected using the same approach described for the validation study, resulting in $P_{\text{size}} = 4000$. The larger population size increases geometric diversity, which is necessary for effective exploration of the expanded star-convex design space. These parameters yield eight optimal solid star-convex solutions corresponding to different values of λ_{desired}.

3.3 Hollow star-convex optimization

The third study extends solid star-convex optimization to include a central hollow region. As shown in Table 3.1, the problem and algorithmic parameters remain unchanged, apart from the hole radius and structural thickness constraints. The range of the allowable hole radii corresponds to hollow regions with areas approximately 3% and 13% of the total cross-sectional area. The structural thickness constraint is selected to be consistent with the minimum thickness observed in hollow fibers manufactured by Shirolkar et al. [2021_Shirolkar]. These parameters result in 16 optimized hollow star-convex cross-sections corresponding to different combinations of λ_{desired} and R_{hole}.

4.0 Experimental validation

A direct method to validate and compare the critical buckling loads of the optimized designs is through experimental compression testing of additively manufactured fiber analogs. These experiments also enable observation of failure mechanisms, including the potential transition between global buckling (governed by I_2) and local lobe buckling (governed by λ). In addition to compressive testing, the fiber analogs are tested in tension to assess any degradation in tensile properties resulting from geometric features of the optimized cross-sections.

A critical metric influencing the mechanical properties of CFRPs is the fiber volume fraction (FVF), which depends strongly on cross-sectional geometry of individual fibers. Ennis et al. estimated FVF by enclosing optimized cross-sections within base shapes with known packing fractions [2022_Ennis]. While effective for the geometries considered by Ennis et al., this approach may be less accurate for the present optimized cross-sections, which feature more pronounced lobes. Accordingly, an experimental approach using fiber analogs is employed to provide a direct comparison of FVF across different cross-sectional geometries.

4.1 Mechanical testing of fiber analogs

Macroscale fiber analogs with circular, triangular, and optimized star-convex solid cross-sections were fabricated using additive manufacturing (AM) and tested under both compression and tension. The analogs were printed using a Formlabs 3 printer with White V4 resin, selected based on preliminary testing for its consistent compressive behavior relative to other AM materials. All analogs had a cross-sectional area of 9.58 mm^2 and an unsupported length of 100 mm. The specimen geometry used for both tension and compression testing is shown in Figure 6.

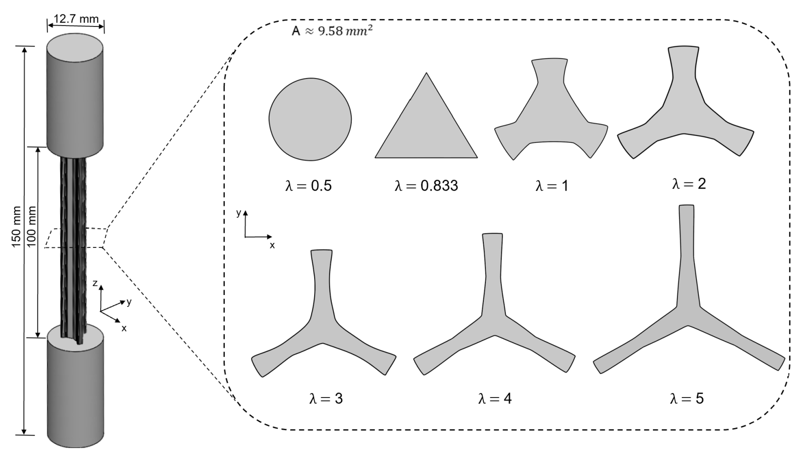

Figure 6: Geometry of the additively manufactured fiber analog specimens used for compression and tension testing.

Mechanical testing was performed using an Instron load frame equipped with MTS V-shaped hydraulic grips. Axial displacement was measured using an EpsilonONE optical extensometer. Compression tests were conducted at a constant displacement rate of 0.18 mm/min until critical global buckling was observed. Tension tests were performed at the same displacement rate until net section tensile failure.

4.2 Fiber volume fraction testing

Macroscale fiber analogs with various cross-sectional shapes were fabricated from Nylon 12 using selective laser sintering. The analogs were 56 mm in length with a cross-sectional area of 9.58 mm^2 and were manually packed into a container with a 50 mm × 50 mm cross-section. After initial loose packing, the container was agitated to promote random distribution. The end faces of the packed fiber analogs were then imaged using a digital camera, and the images were binarized and processed in ImageJ [2025_Rasband] to calculate the projected area occupied by fibers, which was used to estimate the FVF. This procedure was repeated ten times per cross-sectional geometry. To account for the effect of fiber waviness, additional tests were conducted using a mixture of straight and curved fiber analogs. For each cross-sectional geometry, 5-11% of the fibers were replaced with analogs having a constant radius of curvature of 200 mm. The chosen radius of curvature was not based on specific physical observations, but rather selected as a representative value to qualitatively assess the influence of fiber curvature on FVF. The FVF analysis was repeated under these conditions and averaged over ten trials.

5.0 Results and discussion

5.1 Optimal convex cross-section

Figure 7 illustrates the optimization of convex cross-sections aimed at maximizing I_2. The genetic algorithm converged rapidly, identifying the equilateral triangle as the optimal solution within fewer than 130 generations in under two minutes. The evolution of the cross-section demonstrates that the crossover and mutation operators effectively preserved advantageous geometric traits while maintaining sufficient population diversity to explore the design space. The rapid convergence confirms the capability of the optimization framework to identify globally optimal solutions under convexity constraints.

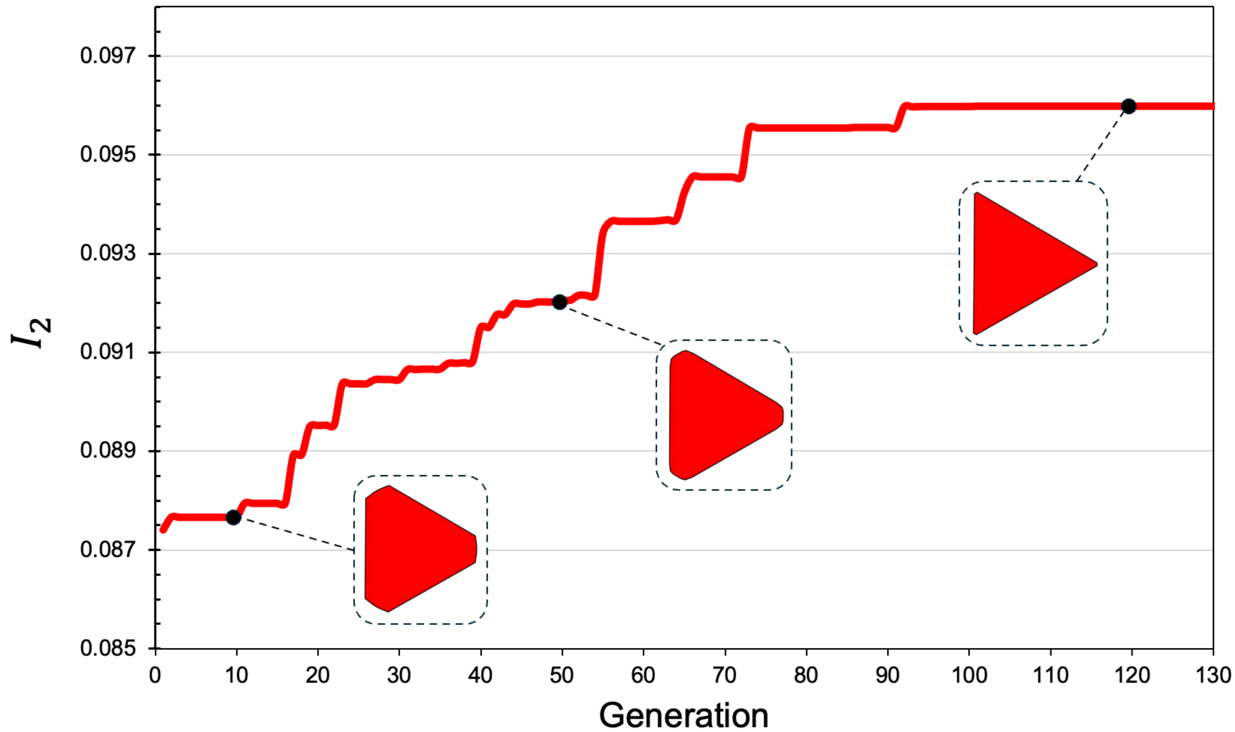

Figure 7: Evolution of the fittest cross-section during convex optimization. The fittest cross-sections are shown at generations 10, 50, and 120. The optimal geometry converges to an equilateral triangle.

5.2 Optimal star-convex cross-sections

Figure 8 shows the evolution of I_2 for solid star-convex cross-sections with $\lambda_{\text{desired}} = 1$ and $\lambda_{\text{desired}} = 4$. Due to the expanded design space, convergence required larger population sizes and over 1000 generations. Qualitative observations of the optimization process indicates that the algorithm initially explores a wide array of geometries before converging toward smooth, high-performance shapes. Optimization of hollow cross-sections ($R_{\text{hole}} \geq 0$) followed similar trends.

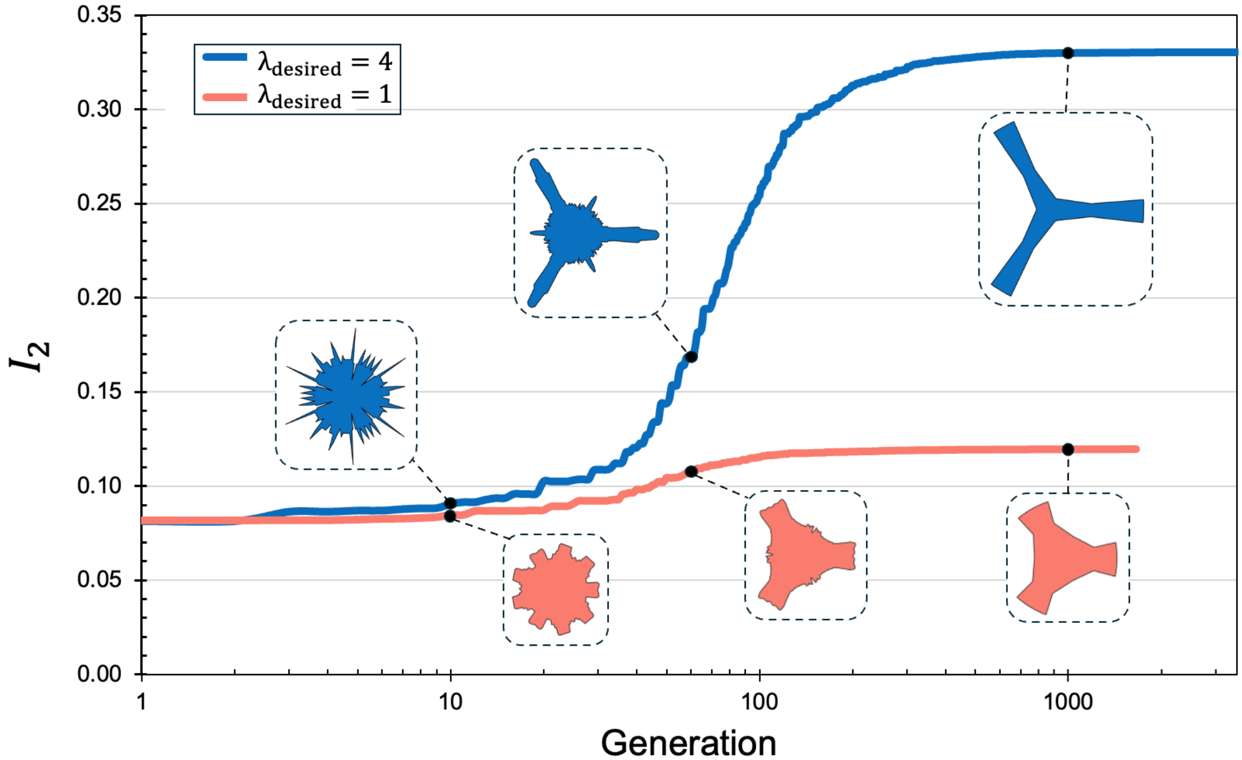

Figure 8: Evolution of I_2 with generation (log-scale) for solid star-convex cross-sections with $\lambda_{\text{desired}} = 1$ and $\lambda_{\text{desired}} = 4$. The fittest cross-sections are visualized at generations 10, 60, and 1000.

Figure 9 presents I_2 for the circular cross-section, selected optimized cross-sections from Ennis et al. [2022_Ennis], and the optimized cross-sections obtained in this study. The optimized cross-sections exhibit a tri-lobed morphology that redistributes material away from the centroid, thereby enhancing structural efficiency. The value of I_2 increases approximately linearly with the imposed aspect ratio constraint, λ_{desired}. The introduction of a central hole further enhances this effect by enabling additional outward redistribution of material. Compared to circular fiber cross-sections, the optimized solid geometries achieve increases in I_2 ranging from 50% to 411%, depending on λ_{desired}. Similarly, hollow geometries exhibit increases ranging from 60% to 440% for $r_{\text{hole}} = 0.1$, and 87% to 484% for $r_{\text{hole}} = 0.2$. Linear interpolation indicates that at the same λ values of 1.66 and 2.23 for the cross-sections from Ennis et al., the optimized solid shapes achieve 37% and 31% higher values of I_2, respectively. Notably, the optimized designs can match or exceed the value of I_2 of the designs from Ennis et al. at substantially lower λ, indicating more compact geometries that may enable higher FVFs in composite applications.

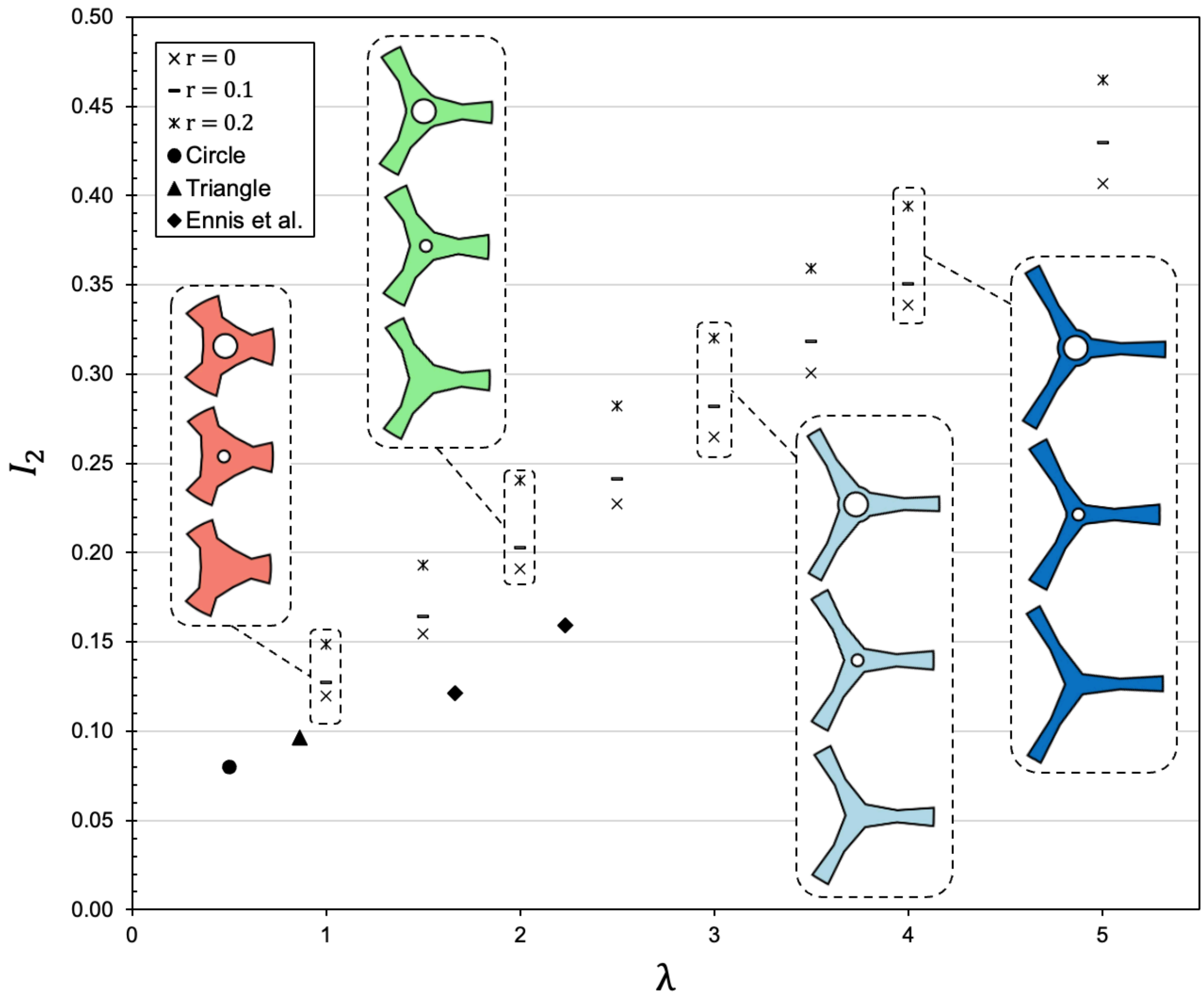

Figure 9: I_2 as a function of the maximum allowable feature aspect ratio for optimized solid and hollow cross-sections. Results are compared with circular and triangular fiber cross-sections, as well as optimal designs from Ennis et al [2022_Ennis].

While increases in λ_{desired} leads to substantial improvements in I_2, the manufacturability of carbon fibers cross-sections with high values of λ can be difficult if not impossible. Cross-sections with λ greater than approximately 2-3 are unlikely to withstand fiber manufacturing processes, the subsequent resin infiltration, and laminate cure. Consequently, from a practical standpoint, the achievable improvements in I_2 for solid optimized fibers may be limited to approximately 230% relative to circular cross-sections. In addition, the optimized geometries produced by the present framework contain sharp edges and corners. In practice, fiber processing is expected to smooth these features, which may reduce the theoretical gains in I_2.

5.3 Mechanical testing of fiber analogs

Figure 10a presents the compression results for the fiber analogs, showing substantial improvements in compressive performance for the optimized cross-sections and a clear positive correlation between λ_{desired} and critical buckling load. The critical buckling load for the optimized fiber analogs with $\lambda_{\text{desired}} = 1, 2, 3, 4$ increased by 37%, 126%, 173%, and 246%, respectively, relative to the circular fiber analog. For optimized fiber analogs with $\lambda_{\text{desired}} > 4$, a transition in failure mode is observed from global buckling to local buckling of the lobes. This transition is characterized by force-displacement softening and a plateau in compressive performance. This is not unexpected, as the fiber analogs are unsupported along their length except at the boundaries. In contrast, fibers in CFRP systems are supported by the surrounding matrix, which is expected to suppress or delay local buckling and promote global buckling of the entire cross-section. This behavior requires further attention and will be the subject of the follow-on work.

Figure 10b compares experimental buckling loads with predictions from Euler buckling theory and linear finite element analysis (FEA). The theoretical predictions follow Eq. 1.1 assuming fixed-fixed boundary ($K = 0.5$) and a Young's modulus of $E = 2.6$ GPa for the Formlabs 3 White V4 resin. The experimental results for fiber analogs with the $\lambda_{\text{desired}} \leq 4$ follow the linear trend predicted by Euler buckling theory and FEA, consistent with the linear relationship between I_2 and the critical buckling load. For fiber analogs with $\lambda_{\text{desired}} > 4$, both experimental data and FEA results show deviation from this trend due to the onset of local buckling.
Tensile testing revealed no significant variation in tensile strength across all fiber analogs, indicating that the optimized cross-section geometries do not introduce substantial stress concentrations that degrade tensile performance.

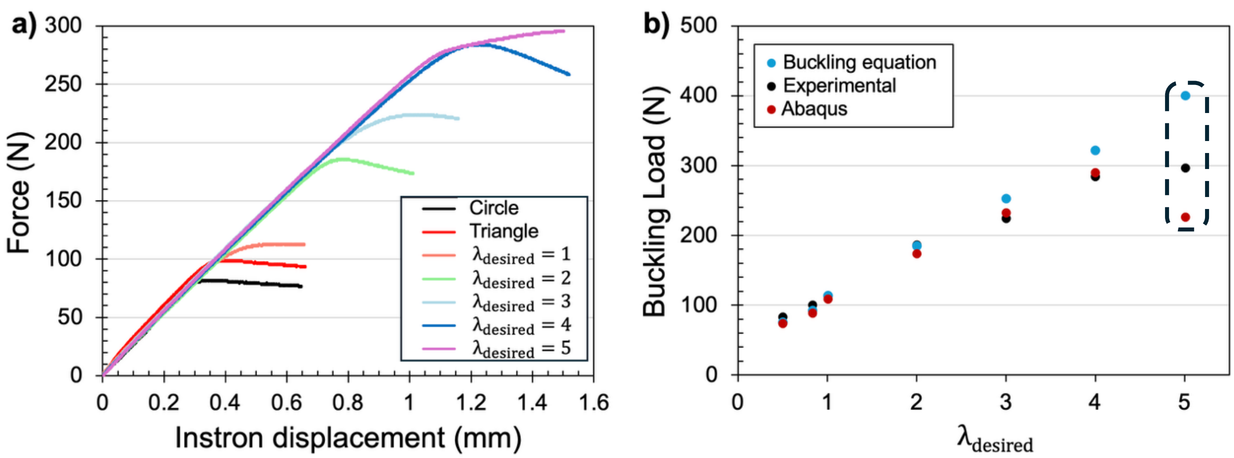

Figure 10: **(a)** Force-displacement response from compression testing of the optimized fiber analogs. Global buckling is observed for all fiber analogs except $\lambda_{\text{desired}} = 5$, which exhibited local buckling. **(b)** Comparison of experimental buckling loads with predictions from Euler buckling theory and linear FEA.

5.4 Fiber packing evaluation

The FVFs of the fiber analogs were evaluated to estimate the packing efficiency of the optimized cross-sectional geometries. Figure 11a illustrates the FVF estimation procedure for circular and $\lambda_{\text{desired}} = 2$ fiber analogs using images of the packed configurations. Figure 11b presents the average FVF for both ideal (straight fibers) and imperfect (mixed straight and curved fibers) packing conditions. For the ideal packing, circular cross-sections achieved the highest FVF of approximately 81%. For reference, the theoretical maximum FVF for circular fibers is 90.7%, while typical prepreg systems exhibit FVFs near 60% [2023_Hexcel], indicating that the present experimental method provides a reasonable upper bound. In contrast, optimized cross-sections exhibit reduced FVFs in the range of 56.3-59% due to the prominence of radially protruding lobes that limit packing efficiency. Imperfect packing conditions, introduced through the inclusion of curved fiber analogs, resulted in lower FVFs compared to ideal packing. However, the FVF under imperfect conditions was not strongly sensitive to fiber waviness.

When considered alongside the compression testing results, a clear tradeoff emerges between critical buckling load and FVF as a function of $\lambda_{desired}$. This indicates that the optimal cross-section geometry depends on the desired balance between compressive performance and packing efficiency for a given application.

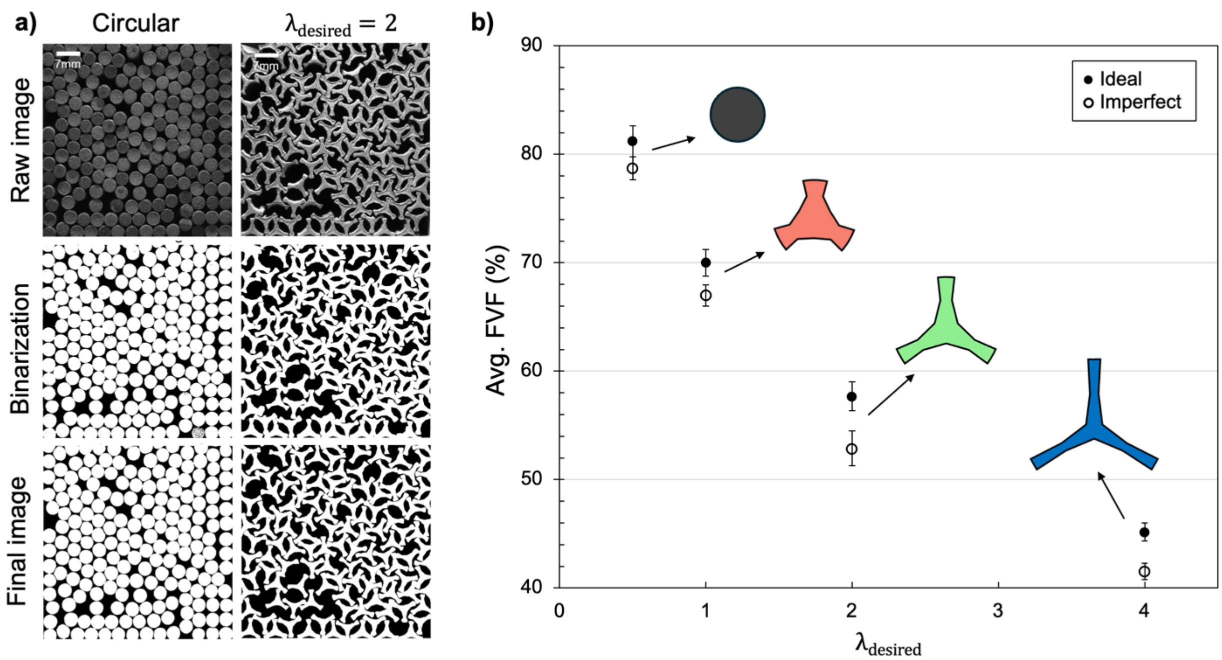

Figure 11: (a) Image processing workflow for estimating FVF from packed fiber analogs. **(b)** Average FVF for circular and optimized cross-sections under ideal (straight) and imperfect (curved) packing conditions.

6.0 Conclusion

This study identified novel carbon fiber cross-sectional geometries that can significantly enhance the compressive performance of carbon fiber-reinforced composites. A genetic algorithm was employed to maximize the critical area moment of inertia, I_2, of the fiber cross-section while satisfying geometric constraints. Implicit constraints enforced star-convex geometries with D_3 symmetry, while explicit constraints controlled cross-sectional area, feature aspect ratio, hole radius, and minimum structural thickness. The key findings of this work are summarized as follows:

- The proposed optimization framework successfully identifies geometry-dependent solutions within a complex, high-dimensional design space.
- Tri-lobal fiber cross-sections emerge as the optimal star-convex geometries for redistributing material away from the centroid to maximize I_2, consistent with prior work [2022_Ennis].

- Both solid and hollow optimized cross-sections significantly increase I_2, with improvements ranging from 50% to over 400% relative to circular cross-sections
- Experimental testing of fiber analogs demonstrates substantial increases in critical buckling load for optimized geometries compared to circular cross-sections.
- Tensile testing indicates no significant reduction in tensile strength due to optimized cross-sectional geometries.
- Optimized geometries result in reduced fiber volume fractions relative to circular fibers, highlighting a tradeoff between compressive performance and packing efficiency.

Beyond identifying optimal geometries, this work establishes fiber cross-sectional geometry as a tunable design variable for improving compressive performance. While the present study relies on macroscale analogs and does not explicitly account for matrix interactions or manufacturing constraints, the results motivate future micromechanical experiments and process developments to assess feasibility in practical composite systems. Incorporating geometric optimization into multiscale composite design frameworks may enable the development of fiber architectures tailored for compressive or multi-directional load-bearing composite applications.

7.0 Acknowledgements

This work was partly supported by The Institute for Ultra-Strong Composites by Computational Design (US-COMP, NASA NNX17AJ32G, a NASA Space Technology Research Institute).

8.0 References

[1] [2012_Rousseau] Rousseau, C., Engelstad, S., Owens, S., n.d. Industry Perspectives on Composite Structural Certification and Design, in: 53rd AIAA/ASME/ASCE/AHS/ASC Structures, Structural Dynamics and Materials Conference. https://doi.org/10.2514/6.2012-1543

[2] [2023_Nunna] Nunna, S., Ravindran, A.R., Mroszczok, J., Creighton, C., Varley, R.J., 2023. A review of the structural factors which control compression in carbon fibres and their composites. Composite Structures 303, 116293. https://doi.org/10.1016/j.compstruct.2022.116293

[3] [1996_Schultheisz_Waas] Schultheisz, C.R., Waas, A.M., 1996. Compressive failure of composites, part I: Testing and micromechanical theories. Progress in Aerospace Sciences 32, 1–42. https://doi.org/10.1016/0376-0421(94)00002-3

[4] [1965_Rosen] Rosen BW, Dow NF. Evaluation of filament-reinforced composites for aerospace structural applications. Philadelphia: NASA; 1965

[5] [1972_Argon] Argon A. Fracture of composites. Treatise on Material Science and Technology 1972:79–114

[6] [1983_Budiansky] Budiansky B. Micromechanics. Comput Struct 1983:3–12

[7] [1990_Fleck] Fleck, N. A. and Budiansky, B. (1990) Compressive failure of fiber composites due to microbuckling, IUTAM Symposium on Inelastic Deformation of Composite Materials, Troy, New York, May 1990.

[8] [1994_Sun] Sun, C.T., and A. Wanki Jun. "Compressive Strength of Unidirectional Fiber Composites with Matrix Non-Linearity." Composites Science and Technology 52, no. 4 (January 1994): 577–87. https://doi.org/10.1016/0266-3538(94)90041-8.

[9] [2009_Pimenta_1] Pimenta, S., Gutkin, R., Pinho, S.T., Robinson, P., 2009. A micromechanical model for kink-band formation: Part I — Experimental study and numerical modelling. Composites Science and Technology 69, 948–955. https://doi.org/10.1016/j.compscitech.2009.02.010

[10] [2008_Uddin] Uddin, Mohammed F., and C.T. Sun. "Strength of Unidirectional Glass/Epoxy Composite with Silica Nanoparticle-Enhanced Matrix." Composites Science and Technology 68, no. 7–8 (June 2008): 1637–43. https://doi.org/10.1016/j.compscitech.2008.02.026.

[11] [2022_Lu] Lu, K., Wang, Z., Li, G., Jiang, R., Sui, G., Yang, X., Zhao, J., 2022. Enhanced longitudinal compressive strength of CFRP composites through matrix stiffening via flexible/rigid epoxide grafted silica: A combined analysis of simulation and experiments. Composites Part B: Engineering 235, 109756. https://doi.org/10.1016/j.compositesb.2022.109756

[12] [2019_Makeev] Makeev, A., Ghaffari, S., Seon, G., 2019. Improving compressive strength of high modulus carbon-fiber reinforced polymeric composites through fiber hybridization. International Journal of Engineering Science 142, 145–157. https://doi.org/10.1016/j.ijengsci.2019.06.004

[13] [1993_Xu] Yong Li Xu, Reifsnider, K.L., 1993. Micromechanical Modeling of Composite Compressive Strength. Journal of Composite Materials 27, 572–588. https://doi.org/10.1177/002199839302700602

[14] [2002_Gardin] Gardin, C & Grandidier, Jean-Claude. (2002). Homogenized models for the modelling of instability in long fibre media. J Appl Mech. 1.

[15] [2009_Pimenta_2] Pimenta, S., R. Gutkin, S.T. Pinho, and P. Robinson. "A Micromechanical Model for Kink-Band Formation: Part II—Analytical Modelling." Composites Science and Technology 69, no. 7–8 (June 2009): 956–64. https://doi.org/10.1016/j.compscitech.2009.02.003.

[16] [2020_Toray] Toray Composite Materials America, Inc. TORAYCA technical manual. Retrieved from, https://www.toraycma.com/wp-content/uploads/Torayca-Technical-Manual_4-28-2020.pdf; 2020.

[17] [2002_Bond] Bond, I., Hucker, M., Weaver, P., Bleay, S., Haq, S., 2002. Mechanical behaviour of circular and triangular glass fibres and their composites. Composites Science and Technology 62, 1051–1061. https://doi.org/10.1016/S0266-3538(02)00035-0

[18] [1960_Keller] Keller, J.B., 1960. The shape of the strongest column. Arch. Rational Mech. Anal. 5, 275–285. https://doi.org/10.1007/BF00252909

[19] [2022_Ennis] Ennis, B.L., Perez, H.S., Norris, R.E., 2022. Identification of the optimal carbon fiber shape for cost-specific compressive performance. Materials Today Communications 33, 104298. https://doi.org/10.1016/j.mtcomm.2022.104298

[20] [2023_Camarena] Camarena, E., Clarke, R.J., Ennis, B.L., 2023. Compressive strength improvements from noncircular carbon fibers: A numerical study. Composites Science and Technology 242, 110168. https://doi.org/10.1016/j.compscitech.2023.110168

[21] [1984_Marín] Marín, J., 1984. Computing columns, footings and gates through moments of area. Computers & Structures 18, 343–349. https://doi.org/10.1016/0045-7949(84)90133-0

[22] [2012_Tsotsis] Tsotsis, T., Haggard, J., 2012. PROCESS OF MAKING A CONTINUOUS, MULTICELLULAR, HOLLOW CARBON FIBER. US8337730B2.

[23] [2015_Gulgunje] Gulgunje, P.V., Newcomb, B.A., Gupta, K., Chae, H.G., Tsotsis, T.K., Kumar, S., 2015. Low-density and high-modulus carbon fibers from polyacrylonitrile with honeycomb structure. Carbon 95, 710–714. https://doi.org/10.1016/j.carbon.2015.08.097
[24] [2021_Shirolkar] Shirolkar, N., Maffe, A., DiLoreto, E., Arias-Monje, P.J., Lu, M., Ramachandran, J., Gulgunje, P., Gupta, K., Park, J.G., Shih, K.-C., Kirmani, M.H., Sharits, A., Nepal, D., Nieh, M.-P., Liang, R., Tsotsis, T., Kumar, S., 2021. Multichannel hollow carbon fibers: Processing, structure, and properties. Carbon 174, 730–740. https://doi.org/10.1016/j.carbon.2020.11.077
[25] [1989_Goldberg] Goldberg, D., 1989. Genetic Algorithms in Search, Optimization and Machine Learning. Addison-Wesley Publishing Company, Inc.
[26] [2004_Haupt] Haupt, R.L., Haupt, S.E., 2004. Practical genetic algorithms, 2nd ed. John Wiley, Hoboken, N.J.
[27] [2025 Rasband] Rasband, W.S., ImageJ, U. S. National Institutes of Health, Bethesda, Maryland, USA, https://imagej.net/ij/, 1997-2018.
[28] [2023_Hexcel] Hexcel. HexTow® IM7 Carbon Fiber: Product Data Sheet. Hexcel Corporation; 2023.